# Exploring ideality and reality in an archetypal rodlike nematic liquid crystal

Louis A. Madsen, 1,2\* Theo J. Dingemans, 1 Chi-Duen Poon, 3 and Edward T. Samulski 1

- 1. Departments of Chemistry and Applied Physical Sciences University of North Carolina at Chapel Hill, Chapel Hill, NC 27599-3300, USA.
- 2. Department of Chemistry and Macromolecules Innovation Institute Virginia Tech, Blacksburg, VA 24061, USA.
- 3. Research Computing Center University of North Carolina at Chapel Hill, Chapel Hill, NC 27599-3420, USA.
- \* Corresponding author. Email: <a href="mailto:lmadsen@vt.edu">lmadsen@vt.edu</a>; Telephone: +1-540-231-1270

This work was supported in part by the US National Science Foundation (NSF) under Award DMR-1810194.

#### Abstract

Numerous theories of molecular ordering in the nematic phase exist that attempt to incorporate the features of weak attractions, excluded volume (aspect ratio), and rigid and non-rigid segments, as well as assess entropic and enthalpic effects. *Para*-quinquephenyl represents a model rodlike molecule, but study of this liquid crystal presents challenges and surprises given the high nematic temperature range. We present NMR experiments throughout the nematic range on two specifically deuterium-labeled quinquephenyl isotopomers, which we combine with high fidelity molecular dynamics simulations to explore and quantify various aspects of orientational order. The striking agreement between experiment and simulation provides new insights into the role of molecular flexibility and correlations (clustering, director fluctuations) on observed order parameters. We compare several nematic theories with our observations and discuss implications for further theoretical understanding.

**Keywords:** deuterium NMR; molecular dynamics; Maier-Saupe; director fluctutations; molecular flexibility

#### Introduction

The underlying phenomena governing the nematic to isotropic (N-I) phase transition and the degree of ordering within the nematic phase have intrigued theorists since the discovery of liquid crystals. Quantitative mean field approaches can be traced back to Onsager's seminal 1949 description of the N-I phase transition based on excluded volume interactions among hard rods[1]. That description was re-formulated as a lattice model by Flory in 1956[2] and soft anisotroptic electrostatic interactions were added a couple of decades later[3]. In 1982 Warner reexamined extant models of the N-I transition and removed the restrictions associated with lattice models (discrete rod orientations) and improved estimates of the athermal limit, the order parameter at the transition and the latent entropy for nematics[4]. But the model that has dominated descriptions of rodlike (calamitic) thermotropic liquid crystals is based on a molecular-field treatment of longrange contributions to the intermolecular potential and completely ignores molecular shape effects—the Maier-Saupe (MS) theory[5, 6, 7]. None of the theoretical models of the N-I transition consider short-range positional order in the nematic phase. Despite its oversimplifications, the MS theory is surprisingly successful in accounting for the temperature dependent evolution of the nematic order below the *N-I* transition for many thermotropic calamitic liquid crystals. Herein we contrast experimental ordering characteristics with theory and simulations using a prototypical calamitic nematogen, p-quinquephenyl (PPPPP; I). This allaromatic, rod-like mesogen without flexible aliphatic appendages (Figure 1) is perhaps the simplest example of a mesogen that closely conforms to model particles underlying theories of the N-I transition. For example, PPPPP was explicitly considered in Warner's comparison of experiment and model[4]. We report the temperature dependence of the molecular ordering using deuterium NMR measurements of two labelled p-quinquephenyl mesogens, PPP-d<sub>4</sub>PP (II) and d-PPPPP-d (III). The phase maps of I – III are shown in Figure 2. A preliminary account of the nematic order measured in d-PPPPP-d appeared in 2006[8], and a further study on unlabeled PPPPP in 2014[9]. Those reported datasets were subsequently contrasted with molecular dynamics (MD) simulations in 2014[10], which gave valuable insights into nematic ordering in PPPPP. In the present paper, we expand on these previous studies by presenting a substantially more comprehensive set of NMR order parameters along with new MD simulations using a highly optimized force-field. We find excellent agreement between experimental measurements and

atomistic molecular dynamics simulations, while existing theoretical models of nematic order below the *N-I* transition differ qualitatively from our observations.

The paper is organized as follows: After a brief review of the thermal properties of unlabeled and <sup>2</sup>H-labeled PPPPP, we present temperature-dependent <sup>2</sup>H NMR data on the C—D bond orientational order for two separate <sup>2</sup>H label positions observed throughout the nematic phase (**Appendix A**). To quantitatively interpret the NMR measurements and extract order parameters, we conducted atomistic MD simulations on PPPPP, which also enable critical insights into the roles of molecular flexibility and correlations on ordering in PPPPP. Finally, we compare these experimental and computational results with several prominent theoretical models of nematics.

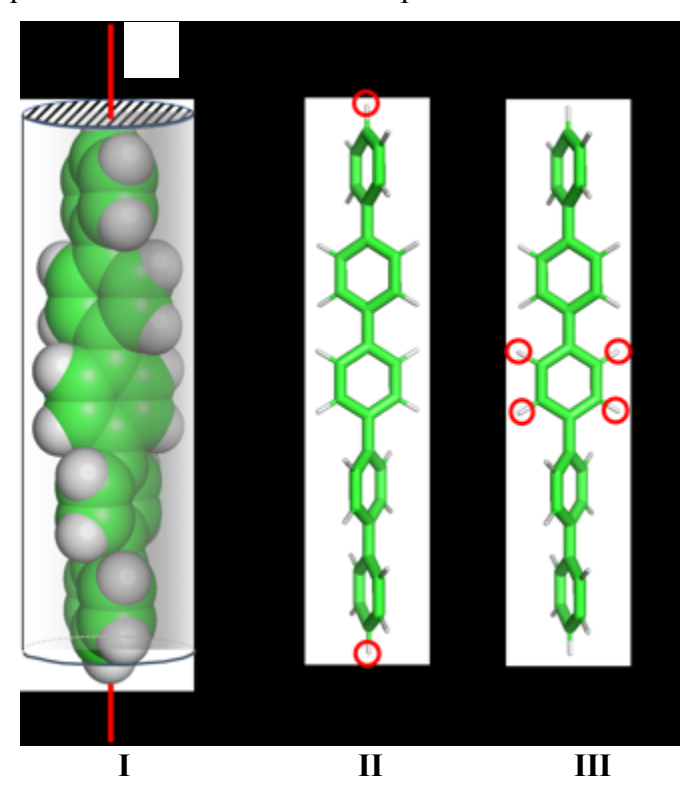


Figure 1. Para-quinquephenyl (PPPP) mesogen molecular structure. Space-filling van der Waals surface (left) has idealized cylindrical shape with an aspect ratio  $\sim 5$ . If this molecule is assumed rigid, its long molecular axis would be readily identified with the para axis of the 'rigid' quinquephenyl mesogen. This work explores the non-rigidity of PPPPP through both NMR measurements and MD simulations. Tube representations (right) show positions of deuterium labels on two PPPPP mesogens.

Cryst	al →	PF → Sr	$nA \rightarrow$	$N \rightarrow$	I
PPPPP (DSC)	≈ <b>623</b>	665	666	698	
PPPPP (MD sims)	N/A	657	663	697	
d-PPPPP-d	≈ 623	663	664	694	
PPP-d <sub>4</sub> PP	≈ <b>623</b>	662	663	700	

**Figure 2. Phase maps for p-quinquephenyl and its isotopomers.** PF is the phenyl ring-flip phase in which quinquephenyl is still solid, but the phenyl rings undergo 2-site rotational jumps. The SmA phase is narrow ( $\sim 1$  K) and only observed in transit via microscopy; N is the nematic phase and I is isotropic. All temperatures are in Kelvin (K). Differences in the transition temperatures reflect isotope effects.

A key message of this work is that at the temperatures explored in the nematic phase of PPPPP (~ 700 K), "toy model" concepts (a rigid molecular fragment or analogies with other aromatic, well-defined molecular geometries) that have been widely employed with success for lower temperature nematics, fail to apply because of the extreme distortions of the PPPPP molecular framework. In other words, at these high temperatures PPPPP is not rigid and indeed does not possess any rigid fragments. **Appendix B** gives the general expressions for interpreting anisotropic NMR interactions in the case of such flexible molecules.

#### **Results and Discussion**

Through the use of two specifically <sup>2</sup>H-labeled PPPPP compounds, we can access a range of order parameter information from quadrupolar and dipolar couplings available via <sup>2</sup>H NMR. **Figure 3** shows the PPPPP molecule and depicts the C-D and D-D geometries relevant to these NMR measurements. The quadrupole interaction gives a measure of the order along the C-D bond axis since the deuterium quadrupole tensor's largest component is oriented along the C-D bond axis[11]. Since we have two different <sup>2</sup>H label positions (central ring for PPP-d<sub>4</sub>PP and *para* end labels for d-PPPPP-d), we have access to two complementary order parameters for *p*-quinquephenyl via the quadrupole interaction. Additionally, the direct dipole-dipole interaction between <sup>2</sup>H on adjacent carbons on the central ring of PPP-d<sub>4</sub>PP gives a measure of the order along the *para*-axis of the central ring, which we define as the **k** axis in the (flexible) PPPPP molecule. Since **S** is a traceless, second-rank tensor, using two of these three distinct order measurements

allows determination of the complete averaged order tensor for a rigid fragment of a molecule. **Appendix A** contains tables of observed spectral splittings and the resulting order parameters as a function of temperature, including the molecular biaxiality parameter. Furthermore, comparisons among these complementary measurements also allow us to comment on the molecular flexibility at these high temperatures.

In order to observe the <sup>2</sup>H-<sup>2</sup>H dipole splittings (due to their small coupling size) we added a <sup>1</sup>H decoupling channel to our NMR probehead to substantially narrow the <sup>2</sup>H spectral lines for PPP-d<sub>4</sub>PP. To reach the high temperature range necessary to probe ordering in PPPPP, we constructed an oven from fumed silica insulation tile and aluminum reflectors in conjunction with a nichrome wire heating element, high temperature thermocouple, and modified RF coil. This oven probe enables stable operation up to 450°C (see *Experimental* section and **Figure 11**), thus giving access to all regions of the PPPPP phase diagram.

We measured the principal component of the quadrupolar splitting tensor for the C-D bond in the two labeled compounds by conducting solid-state wideline (static sample)  $^2$ H NMR on powders of each sample at room T. Both PPP-d<sub>4</sub>PP and d-PPPPP-d showed clean 3D powder patterns, with the d-PPPPP-d spectrum shown in **Figure 4a**. The quadrupole splittings of the C-D bonds (for each molecule) aligned directly with the spectrometer field are 254.8 ( $\pm$  1.0) kHz for PPP-d<sub>4</sub>PP and 256.0 ( $\pm$  1.0) kHz for d-PPPPP-d. The asymmetry of the quadrupolar coupling is too small to reliably measure by fitting the spectrum (see below and **Appendix A**). The solid-state  $^2$ H spectrum of the PPP-d<sub>4</sub>PP compound at 355°C (**Figure 4b**) shows the partially averaged powder spectrum resulting from fast phenyl ring flips at this temperature[12].

We note that upon studying the d-PPPPP-d molecule in the N and I phases at ~ 700 K (~400°C), we observed  $^2$ H label exchange with other  $^1$ H atoms on PPPPP. This manifested as a continuous decrease in the intensity of the d-PPPP-d quadrupolar lines and increase in splittings similar to those for PPP-d<sub>4</sub>PP (*meta* and *ortho*) positions. After ~ 10 hours, approximately 90% of the end *para* label signal intensity became depeleted, and corresponding area signals for meta and ortho labels appeared. We would expect that the  $^2$ H- $^1$ H exchange would only happen on the terminal phenyl rings, although the large NMR signal intensity changes suggest that exchange may occur with other ring hydrogens as well. While these observations fall outside the scope of this article, we believe this is an as-yet unobserved phenomenon in aromatic H-D exchange and thus worthy of further study.



Figure 3. PPPPP diagram with orientation and  ${}^{2}H$  label geometries relevant to NMR measurements.  $\theta$  is the angle of the C-D bond with respect to both the nematic director n and the magnetic field  $B_0$  (in the PPP-d<sub>4</sub>PP compound), relevant to calculation of S using NMR data.  $r_{DD}$  is the internuclear D-D vector that determines the size of the dipolar interaction between the central ring  ${}^{2}H$  nuclei. The D labels at the ends of the d-PPPP-d compound would, for a rigid molecule, be along the para axis of the molecule. Thus, we have three independent measures of nematic order parameters, as well as allowing experimental assessment of molecular flexibility. Note that these angles are only relevant with respect to n and n0 and not to intramolecular coordinates, owing to the flexibility of the PPPP molecule, which we will discuss in detail below.

By combining the principal component of the quadrupole tensor (**Figure 4**) with temperature-dependent quadrupole spectra of each labeled PPPP molecule, along with the geometry of each C-D bond within the respective molecule, we can construct order parameter curves throughout the nematic phase.

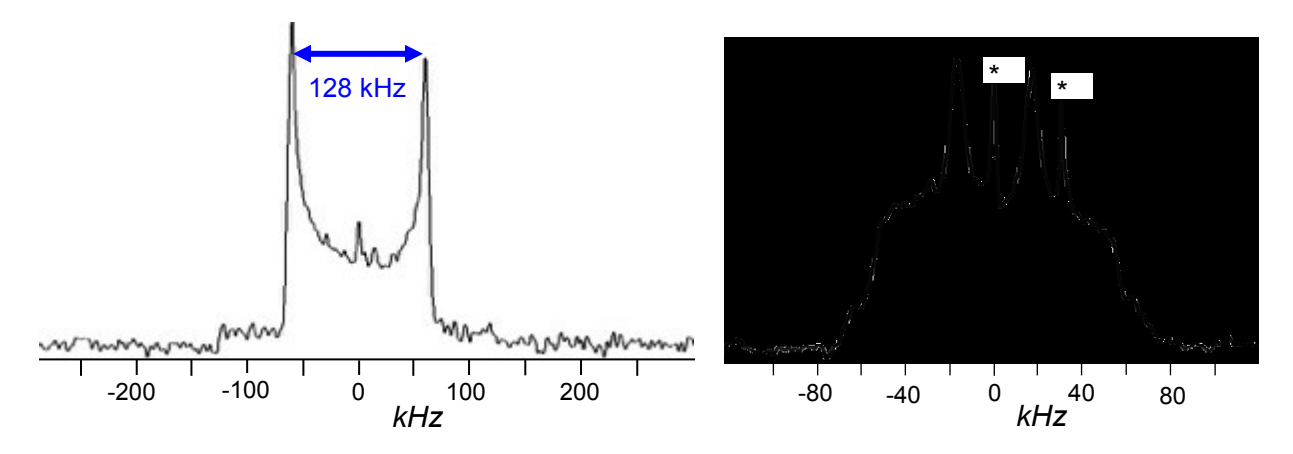
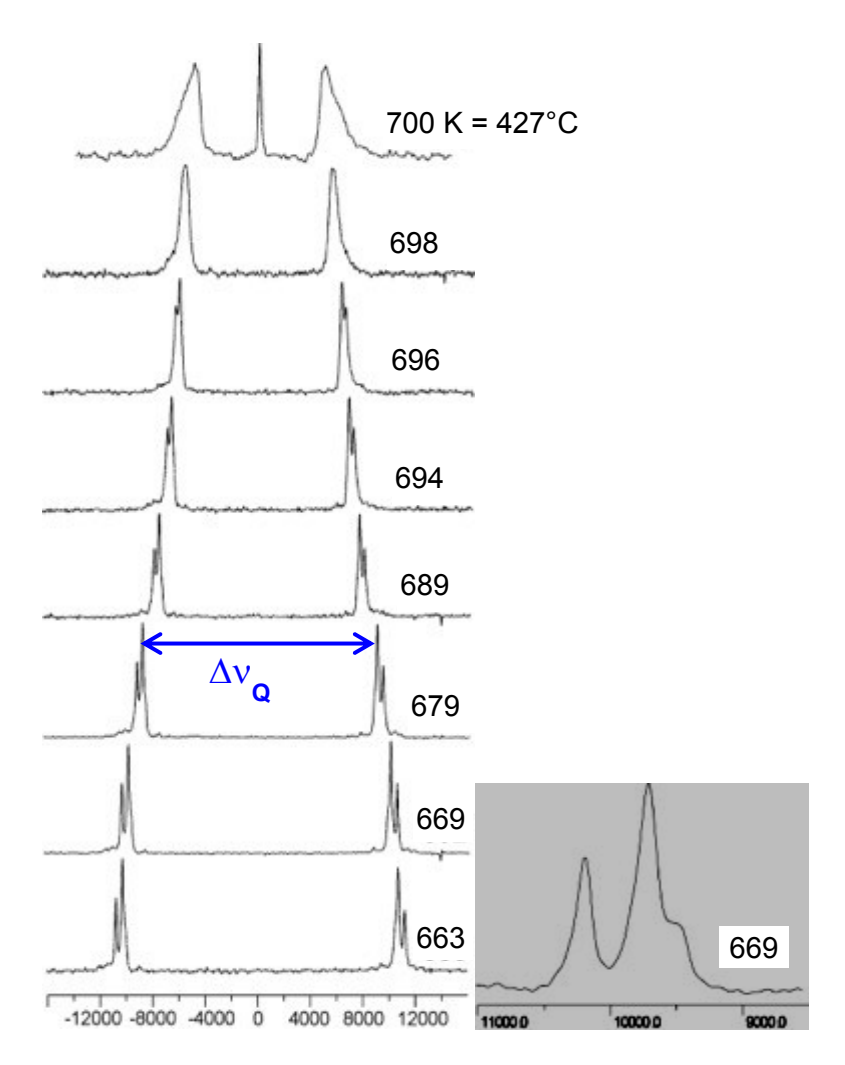


Figure 4. Solid-state wideline <sup>2</sup>H spectrum (298 K, *left*) for d-PPPP-d and phenyl ring-flip (*PF*) phase spectrum (628 K, *right*) for PPP-d4PP. We use a solid echo ( $90_x - \tau - 90_y - \tau$  - acquire) to record these spectra. We extract the principal component of the C-D quadrupole tensor  $Q_p$  from the room T crystal spectrum by measuring between the Pake doublet "horns" and multiplying by two. The spectrum at right shows partial averaging of the C-D couplings in powdered PPP-d<sub>4</sub>PP due to rapid ring flips about the *para* axes of the molecules. Note the peaks marked by asterisks (\*) are noise peaks from the spectrometer, mostly resulting from coupling of noise into the RF coil via the oven shielding. Note that the horizontal scale for the *PF* spectrum is twice as large as for the solid-state spectrum. The overall width of the observed ring-flip spectrum reduces by a factor of two relative to the room T crystalline powder spectrum due to partial averaging of the quadrupole couplings, solely from the effect of the ring rotations and no other motional averaging process (molecular tumbling or diffusion)[12].

**Figure 5** shows 1D  $^2$ H NMR spectra covering the nematic range for PPP-d<sub>4</sub>PP. When acquiring simple  $^2$ H spectra, the dipolar coupling to the  $^1$ H nuclei on adjacent rings caused significant linebroadening ( $\approx 2.5$  kHz FWHM). Thus, we added a simple  $^1$ H channel that enabled CW decoupling at 6 kHz bandwidth (nutation frequency), thus removing the  $^1$ H- $^2$ H dipolar couplings and reducing  $^2$ H linewidth to 200 Hz FWHM. We employed theory developed by Poupko *et al.*[13] to analyze the dipolar splitting patterns and extract both the true  $\Delta v_Q$  quadrupolar couplings as well as the  $^2$ H- $^2$ H dipolar couplings. Note that we observe a true first-order phase transition at 700 K (427  $^{\circ}$ C), where a  $\approx 2$  K spread across the sample causes coexistence of *N* and *I* spectral components, but not in a continuous manner.



**Figure 5. Proton-decoupled** <sup>2</sup>**H NMR spectra of PPP-d<sub>4</sub>PP.** Within the *N* phase, quadrupole splittings increase from 8 kHz to 22 kHz upon lowering temperature. In order to resolve the dipolar coupling fine structure within the quadrupolar split doublet peaks, we added an untuned <sup>1</sup>H channel to the single NMR coil and applied continuous-wave (CW) decoupling with a nutation frequency of 6 kHz. The inset shows the <sup>2</sup>H dipole-dipole (DD) coupling pattern of each peak of the quadrupolar doublet. Without decoupling, the linewidth of the quadrupolar peaks is 2500 Hz at the bottom of the *N* phase due to protons with distributed angles on adjacent rings, and linewidth = 200 Hz with decoupling. This decoupled linewidth dominates the error bar for the quadrupole splitting values at  $<\pm1\%$  in the lower 3/4 of the *N* phase. The static spread in temperature across the sample (≈ 2 K, from coexistence of *N* and *I* phases) combined with the stronger dependence of  $\Delta v_Q$  nearer to the *I* phase determines the error bar (up to  $\pm5\%$ ) for the splittings at higher T.

Concerning the asymmetry or biaxiality of the electric field gradient (EFG) tensor ( $\eta_{EFG}^{CD}$ ) and the PPPPP molecule: The value for  $\eta_{EFG}^{CD}$  for known aromatic deuterons is small[14, 15] (~0.05) and a quantitative determination of the particular  $\eta_{EFG}^{CD}$  for PPPPP would require a much more careful analysis and is beyond the scope of this work. For the purposes of this study, we have assumed the EFG tensor to be uniaxial, and we have tabulated the molecular biaxiality parameters extracted from the C-D quadrupolar and D-D dipole-dipole NMR measurements on PPPd<sub>4</sub>PP in **Appendix A**.

To understand our NMR measurements of PPPPP order parameters, we also conducted a detailed molecular dynamics (MD) simulation study on this molecule. Our initial goal was to simply obtain the average angle of the C—D bond on PPP-d<sub>4</sub>PP relative to the molecular long axis, and we presumed the terminal C—D bonds for d-PPPPP-d would be coincident with that axis. However, at the ~ 700 K temperatures encountered in the nematic phase, issues of intramolecular flexibility impact the specification of the "molecular long axis" (see below). Also director fluctuations can affect interpretations of the NMR data. However, all of these contributions to averaging the C—D bond vector relative to the magnetic field direction are subsumed into the calculation of the bond order parameters S<sub>C-H</sub> via the method of Eppenga and Frenkel[16, 17], up to the scale of the MD simulations (see additional discussion below). In brief, we conducted this MD study on 1000 molecules on the 10 ns timescale using the GROMACS software platform and with a modified OPLS-AA force field. We determine the S<sub>C-D</sub> order parameters as the maximum eigenvalues of the Saupe ordering matrix of the respective C-D bond vectors at every point in the MD trajectory. The respective eigenvector is the nematic director. (The other two eigenvalues are found to be essentially identical, reflecting the uniaxiality of the phase—in other words, the physical equivalence of the directions defined by other two eigenvectors.)

We can further infer the quality of the force field we employ in the MD simulations from a plot of the simulated density versus absolute temperature, as shown in **Figure 6**. The agreement between simulated transition temperatures and the experimental ones is remarkable (**Figure 2**). The force field parameters were carefully optimized solely to reproduce measured density data for PPPP[18] and with incorporation of the latest understanding of simulated intermolecular interactions in phenyl-ring-dominated systems (see *Experimental* section).

In order to anticipate ordering based on MD simulations, we can explore the simulated order parameter  $P_2$ , which we term  $S_k$ , where k is the instantaneous vector connecting the *para* carbons of the cental ring) and the associated higher order parameter  $P_4$ . Figure 7 shows these two order parameters as a function of reduced T along with snapshots of molecular configurations at representative points along these curves. The MD simulations show the N phase spanning 663 K to 697 K, and we define reduced T here as the absolute temperature T over the nematic-istropic transition temperature  $T_{NI}$  (see Figure 2) or  $T/T_{NI} = T/697$  K. Starting in the crystal phase, PPPPP molecules are three-dimensionally packed, with prominent 2D layers apparent (653 K snapshot shown). Melting into the narrow SmA phase, we see that 2D layering is still present. Upon melting into the N phase (664 K snapshot), we see strongly oriented molecules along a director, with perhaps more significant local ordering across the simulation box (size  $\approx 10$  nm) than one might expect. In the nematic near the  $T_{NI}$  melting point (695 K), we see smaller locally ordered clusters and we cannot readily observe a clear director n, and this snapshot looks quite similar to points just above  $T_{NI}$  (700 K). Higher into the I phase, we still see small local clusters of PPPPP molecules, as expected for an isotropic liquid formed from a highly anisotropic molecule.

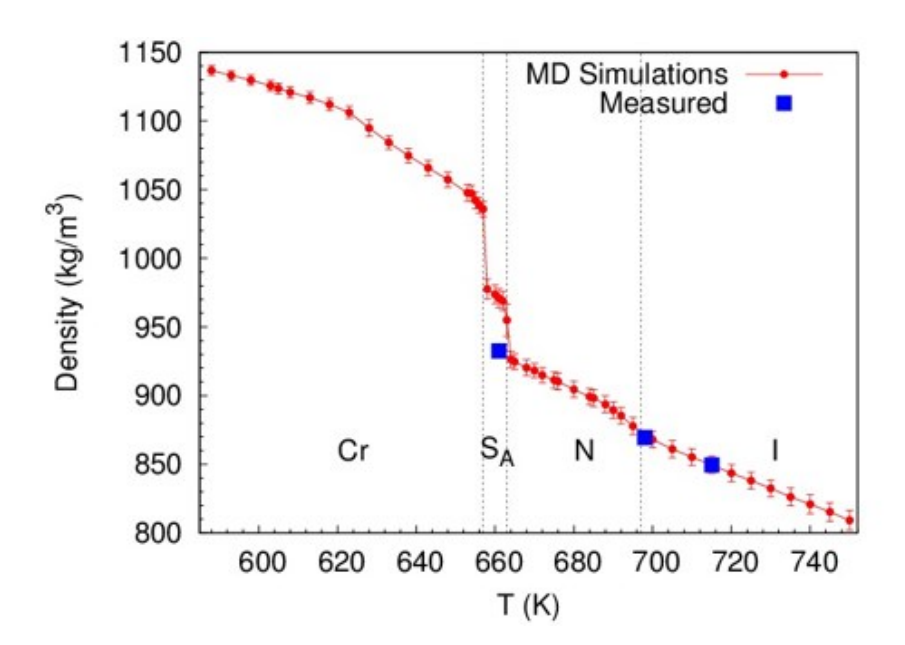


**Figure 6: Density from MD simulations vs absolute T.** The verical dotted lines are derived from the MD simulated transition temperatures (see phase map for PPPPP – Figure 2). The deviations between experimental nematic transition temperatures and simulations are < 4 K.

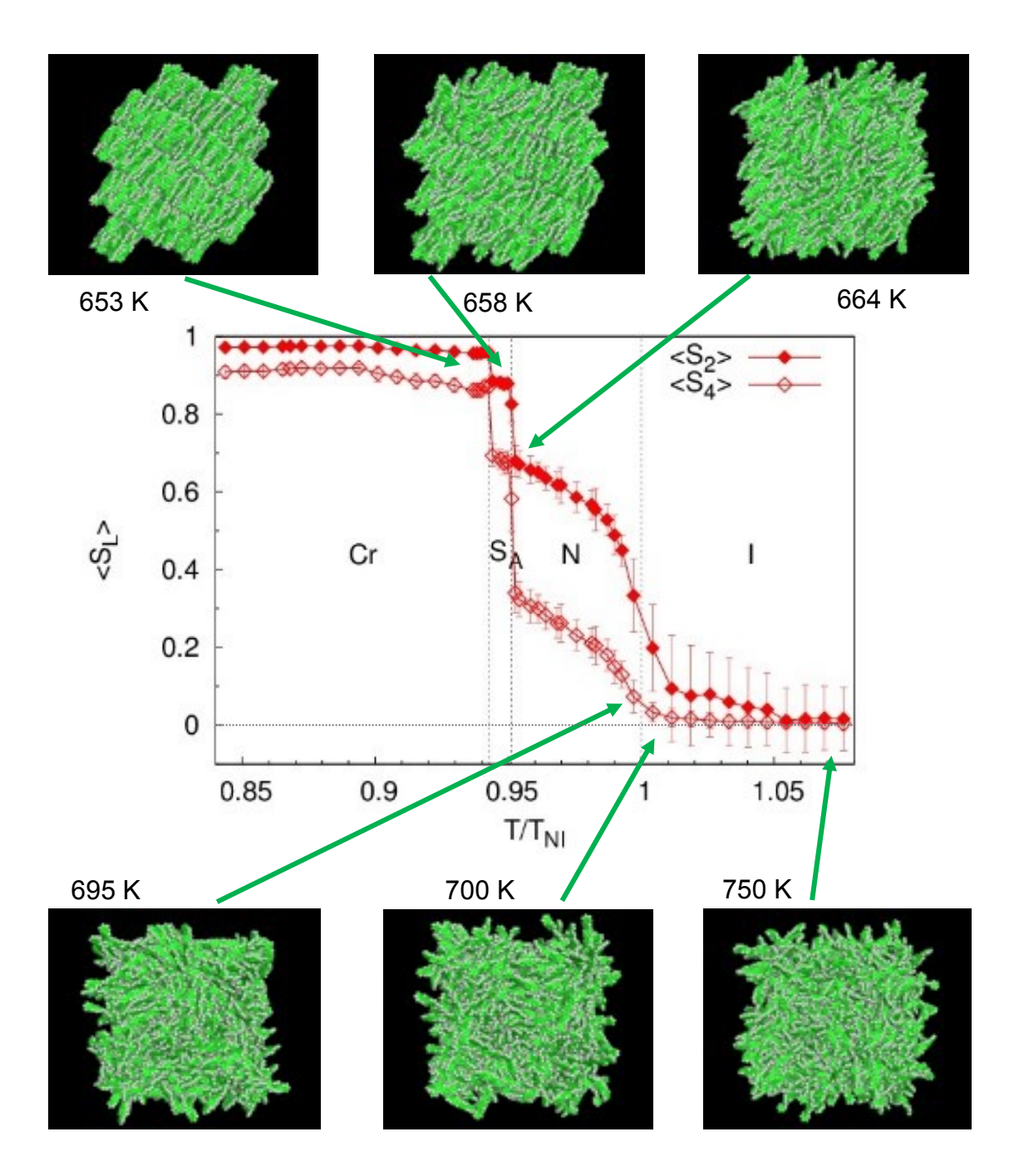
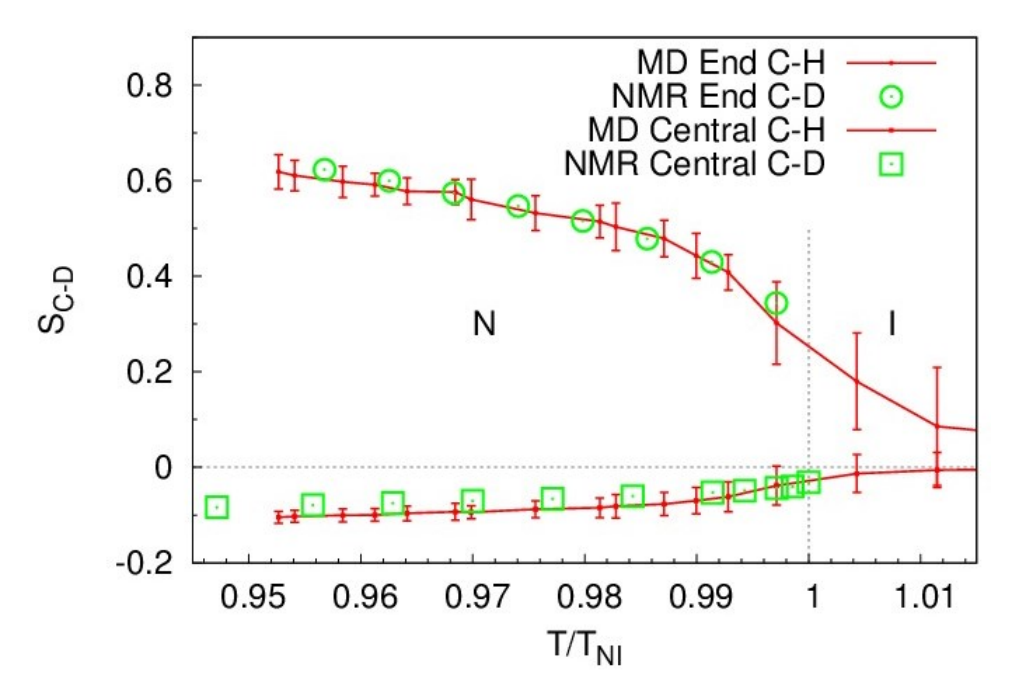


Figure 7. MD simulations of <P<sub>2</sub>> and <P<sub>4</sub>> order parameters for the central ring *para* axis k with representative configurations of the PPPP molecules.

**Figure 8** shows measurements of the  $P_2(\cos\theta)$  (or  $S_{C-D}$ ) order parameters extracted from the <sup>2</sup>H NMR quadrupole splittings (circles and squares, errors smaller than symbol size) for the PPP-d<sub>4</sub>PP and d-PPPP-d plotted along with MD simulations (small data points, with error bars) for each bond position ( $S_{C-H}$  for central ring C-H and end ring *para* CH), all as a function of reduced

temperature T. Note that we quantify  $T_{\rm NI}$  separately for MD simulations, and experimentally via DSC for each labeled mesogen, d-PPPP-d and PPP-d<sub>4</sub>PP. These curves show excellent agreement throughout the entire N temperature range, an observation that carries implications for the relationship between order measurements with NMR and the internal dynamics, director fluctuations and relative alignment of the PPPPP molecules.



**Figure 8.** Order parameters of PPP-d<sub>4</sub>PP and d-PPPP-d from NMR and MD simulations. We measure C-D bond order parameters from NMR quadrupole splittings for each label position (See **Table 1**). MD simulations yield C-H bond order parameters at these same positions. The NMR measurements (circles and squares) have errors ≤ symbol size.

The MD simulations have a time duration of 10 ns and employ a box size of 10 nm. On these and shorter time scales, order parameters derived from the simulations account for all features of molecular flexibility and director fluctuations. To derive the order parameters from certain measured NMR splittings (quadrupolar and dipolar), we are using geometric parameters from the simulations, *e.g.*, for PPP-d<sub>4</sub>PP the D-D internuclear distance and the C-D label angle with respect to the nematic director (along the spectrometer  $B_0$  field). The NMR splitting measurements in the *N* phase, on the other hand, correspond to a time scale of the inverse of the observed quadrupole splitting, which is  $t_{\rm NMR} \sim 1/(10 \text{ kHz})$  or  $\sim 100 \, \mu \text{s}$ .[19, 20, 21, 22] The length scale of the measurement depends on the average displacement of PPPPP during this time, or  $t_{\rm RMS}$ 

 $\sim \sqrt{6Dt_{NMR}}$ , which depends on the molecular diffusion coefficient D.[20, 21, 23] For simplicity, we assume an average isotropic diffusion coefficient and 3D diffusion. From the simulations, we find  $D \sim 2 \times 10^{-9}$  m<sup>2</sup>/s (see **Appendix D**) and so the length scale for NMR is  $r_{\rm RMS} \sim 1$  µm. Thus, the close agreement between order parameters for the end C-D label positions probed by NMR in d-PPPPP-d and the central label positions in PPP-d<sub>4</sub>PP, and the same bonds probed by MD simulations (Figure 8) strongly suggest that any fluctuations (such as director flucutations) that are important for agreement between MD and NMR must be at or below the length/time scales sampled by the MD sims (10 ns and 10 nm). In other words, dynamic director fluctuations on larger length scales and longer time scales must not be affecting, or contributing to the motional averaging of, the NMR order measurements, which are averaged over quite slow time scales (~100 us). A static distribution of directors (variable domain orientations) also must have a minimal effect on NMR order measurements. This conclusion is also apparent in the NMR linewidths, which are  $\sim 1\%$  of the quadrupole splitting  $\Delta v_Q$  value at the low T end of the nematic range. The linewidth does increase nearer to  $T_{\rm NI}$ , but we assign this variation to a static temperature gradient across the sample combined with the strong temperature dependence of the order parameter when approaching  $T_{\rm NI}$ .

Next we compare these experimental and simulation results with relevant theories of nematic order. Maier-Saupe (MS) theory assumes a simple  $P_2$ -dependent molecular interaction potential and does not specify, e.g., the specifics of the interaction or the aspect ratio of the molecules. Luckhurst and Picken postulated the extended Maier-Saupe (EMS) theory,[24] which takes into account effects of varying molar volume in an adjustable scaling factor, and this theory yields a stronger dependence of S vs. reduced temperature than MS. Warner explicitly calculated the temperature dependence of  $S_k$  for PPPPP and his model incorporates both attractive interactions as well as excluded volume, including the effect of molecular aspect ratio.[4] **Figure 9** plots our  $^2$ H NMR and MD simulations data along with the MS theory as a function of reduced T, the EMS theoretical curve (with the maximum physically meaningful scaling exponent of 3) and the Warner theory. The T dependence of all three theories deviate substantially from the experiemtnal  $S_{C-D}$  order parameter determined using NMR, especially near the T-T transition. Note that the MD simulation of T in **Figure 9** is a measure of the orientational order of the central ring T para axis T (the configuration-dependent vector connecting the T-carbons of the central ring). T

differs from the end C-H bond position in **Figure 8**, where we show the directly simulated C—H bond order parameter ( $S_{C-H}$ ). Hence, the experimental data from d-PPPPP-d is also substantially lower than the simulated  $S_k$  because it is averaged by the intramolecular flexing of the molecule at these elevated temepratures. Here we note that there are no constraints imposed on any degrees of freedom of the system in this MD simulation. All modes are completely active, and thus any conceivable type of molecular flexibility is represented in these simulations. While the EMS theory with the maximum scaling exponent of 3 shows the closest agreement with our MD results across much of the N phase, it deviates substantially as the NMR and MD curves sharply decrease when approaching  $T_{NL}$ . For the Warner theory, note that we have digitized and inserted this curve from the original reference, and we have located the inflection point (slope approaches infinity) at  $T_{NL}$ . The Warner theory qualitatively captures the stronger slope decrease of  $S_k$  when approaching  $T_{NL}$ , but underestimates the slope of the S curve deeper into the N phase.

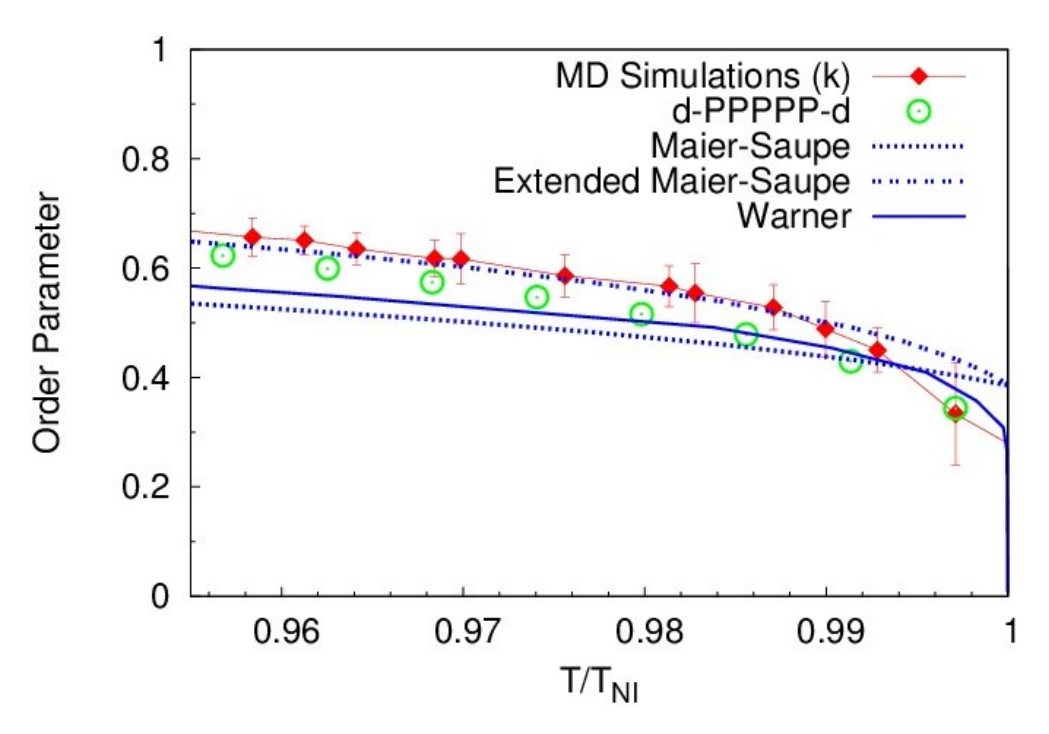


**Figure 9: NMR and MD simulations of order parameters along with theoretical curves**. The experimental values (green circles) are from the NMR data on d-PPPPP-d, and the simulations are from the **k** axis (*para*-axis of the central PPPPP ring).

What factors contribute to these large discrepancies between theory and experiment? Our initial thoughts were that director fluctuations (static and/or dynamic) might account for these

discrepancies. We can essentially rule out those effects based on the agreement between high fidelity MD simulations and quadrupolar NMR (**Figure 8**), and based on the narrow NMR linewidths and  $\sim 1 \mu m$  diffusion length for  $^2H$  NMR experiments. Furthermore, since PPPPP has no flexible aliphatic appendages, it ideally enables testing of simple nematic order theories without the uncertainty of flexible aliphatic chain-chain considerations. However, since the *N* phase exists at such high *T*, we can expect that molecular flexibility of this all-aromatic backbone is a significant concern for this otherwise ideal mesogen. In order to infer some features of intramolecular flexibility, we can consider a single molecule from the MD simulation at 400°C (**Figure 10**). Clearly, we can observe large distortions of the aromatic molecular backbone, which we would otherwise consider to be highly rigid at room *T*. This gives us a visual understanding of how our measured and simulated order parameters relate to molecular flexibility. We can imagine asking a number of questions regarding how this flexibility propagates in different experimental measurements of order, and high fidelity MD simulations such as these provide a powerful toolkit for understanding relationships between flexibility, aspect ratio, mesogen shape, and observed order.



**Figure 10:** Instantaneous conformation of a single molecule at 670 K. This MD simulation snapshot shows flexibility of the "para axis" of PPPPP relative to the central ring para axis k. We define k as the instantaneous vector (red line) connecting the two para C atoms of the cental ring.

The observations of significant flexing of PPPPP at these high temeratures could also suggest that short-range packing of the PPPPP molecules – positional order in the nematic – may be convoluted with the flexible configurations. Varying effects of molecular packing[18, 25, 26, 27, 28] – short range positional order across the nematic phase but especially near the *I-N* transition, due to different dependencies of excluded volume vs. attractive interactions – may drive the observed temperature dependence of the order parameter. We also note that we observe a small (but within errors of zero) biaxial molecular order in our PPP-d<sub>4</sub>PP NMR measurements and a small but non-significant phase biaxiality in MD simulations (see **Appendix A**). This suggests that the importance of local correlations in the overall behavior of the PPPPP nematic phase is not significant.

In the end, none of the first-principles theories of nematics can account for the experimental and simulations data on PPPPP. Investigating order in this otherwise archetypal example of a nematic leads us to conclude that any simple, basic theory of nematics will be subject to the particulars of intermolecular attractions, molecular aspect ratio and shape, molecular flexibility, and temperature dependencies of such attributes. Theories that incorporate entropic vs. enthalpic and excluded volume vs. attractive interactions[4, 27, 28, 29] can serve to fit some experimental dependencies, but often fall short of a clear picture of what interactions give rise to measured ordering for arbitrary molecular systems. Modern MD simulations provide the most compelling path to disentagling the effects of molecular flexibility and/or local correlations or fluctuations. Using MD, we can freely select and modulate which interactions, clusters, and geometries we include in the nematic/molecular model, and we can extract order parameters from experimental data with more specific geometrical and dynamical information.

### **Conclusions**

This study presents new insights into the PPPPP nematic based on comprehensive NMR order parameter data for two  $^2$ H label positions complemented by cutting-edge MD simulations. Flexing of the PPPPP molecular backbone, which is substantial at the high temperatures of the nematic phase, represents a key feature of the ordering investigated by NMR and simulations. The general agreement between simulated and experimental  $S_{C-D}$  is impressive and reinforces our use of an optimized force field in MD simulations to gain insights from experimental results. The detailed differences between theory and experiment (**Figure 9**) may point to a common issue with

all of the theories – a failure to consider short range positional order (cybotaxis) in the nematic. The clear departure of linearity of PPPPP at these elevated temperatures may exacerbate near-neighbor orientational correlations in the nematic and those correlations are probably made more facile by local stratification. A sensible near-term study on systems like *p*-quinquephenyl will include investigating cybotaxis, including correlation length dependencies on molecular attractions and aspect ratio, as well as the effects of local ordering and local biaxiality on phase behaviors and phase transitions. Correlated local bending fluctuations may also play a significant role in phase behavior, and this model liquid crystal may provide a tractable model system for deeper understanding of room temperature nematics with built-in flexible (*e.g.*, alkyl) subunits.

## Experimental details

Synthesis of labelled *p*-quinquephenyl molecules: We explain these procedures in detail in Appendix C.

High temperature NMR apparatus: We modified broadband solids (X) probehead (Bruker-Biospin, Billerica, MA), as shown in **Figure 11**, This high temperature oven is capable of up to 450°C (720 K) operation with no need for active cooling of the probehead. Fumed-silica tile as used on the outer hull of NASA's Space Shuttle comprises the insulating walls of our oven, and a skin of aluminum foil (heat shield) attached with ceramic cement (Omega 600 High T Cement) reduces radiative losses to keep the outer shell below 70°C. The cylindrical oven is 6.5 cm tall by 6.5 cm diameter with a 1.4 cm minimum wall thickness. The spectrometer's variable temperature controller (Bruker BVT 3000) drives a ~ 4 Ohm nichrome heating coil (Omega Ni80-012, 300 µm diam. wire), and reads temperature using a type-E thermocouple (Omega) situated within 4 mm of the sample edge. The base of the nichrome heating coil and the thermocouple is held by cement to the oven base after punching them through the tile. At 400°C, the temperature precision is +/- $0.2^{\circ}$ C and the spread over a 3 mm diameter sample is  $\approx 2^{\circ}$ C. Sample equilibration after setpoint changes of < 10°C occurs in < 2 min. The NMR RF coil consists of a 13 turn tin-plated 22 gauge copper wire tuned to <sup>2</sup>H frequency (55.2 MHz), wound to produce an inside diameter of 5.5 mm. We punch the RF coil leads through the silica tile before soldering to the SMA connector plugs that interface with the Bruker probe electronics, and prior to cementing the leads to the tile surface on the inside and prior to attachment of the outer aluminum heat shield. The upper oven assembly (walls and top – see Figure 11) is held down to the main probe body by ordinary rubber bands

looped around small screws on the sides of the Teflon® probe base. The probe assembly enables observed <sup>2</sup>H linewidths of < 30 Hz FWHM, with shimming done in the isotropic phase with proton signals before recording LC-phase spectra.



Figure 11: High temperature NMR apparatus. We fabricated this oven atop a wideline, widebore, broadband (X) probe from fumed silica tile with aluminum foil reflectors anchored by water-based cement (Omega 600 High T Cement). This apparatus can maintain sustained sample temperature up to 450°C (720 K). The heating elements are spiral wound NiCr wire, which flank the tin-coated copper 13-turn NMR coil. An E-type thermocouple (Omega) sits  $\approx 4$  mm below the NMR coil, and no forced air passes through the oven interior. We achieve typical shim-limited linewidths of 20 Hz on a 4 mm ID spherical-bulb D<sub>2</sub>O sample. Maintaining T = 680 K ( $\pm 0.2$ °C average) requires < 8% of the Bruker VT-3000 heater maximum power.

**Solid-state NMR:** We used a solid-echo pulse sequence  $(90_x - \tau - 90_y - \tau - \text{acquire})[30]$  with a 90° pulse time of 2.0 µs and  $\tau$  delays of 17 µs to acquire the powder pattern spectra in the solid state. After simple tuning with a pulse-acquire experiment, we found that  $T_1 \sim 100 \text{ s}$  in the solid phases, so we used a relaxation delay of 100 s and 2048 scans for each spectrum.

**LC-phase NMR:** We recorded all liquid crystal phase and isotropic phase spectra using a 1D pulse-acquire experiment (since the broadest bandwidth needed was  $\cong 20 \text{ kHz}$ ) and with a 90 pulse time of 2.4 µs.  $T_1 \sim 1 \text{ s}$  in the liquid crystal and isotropic phases, so we used a relaxation delay of 2 s and 1048 - 4096 scans per spectrum.

We collected all NMR data except the room temperature crystal phase spectrum using a Bruker DRX 8.45 T (360 MHz for <sup>1</sup>H) spectrometer, which is 55.2 MHz for <sup>2</sup>H. Bruker-Biospin collected the crystal spectrum on an 11.7 T Avance II spectrometer operating at 76.8 MHz for <sup>2</sup>H.

Molecular dynamics simulations: We performed molecular dynamics of PPPPP using the OPLS-AA force field. We utilized the LigParGen web server[31] to construct the initial OPLS-AA force field for PPPPP. We modified the initial OPLS-AA force field in 3 ways. To modify atomic charges in the force field, first, we optimized the geometry using the Jaguar in Materials Studio program suite (version 2018, Schrodinger, LLC, New York, NY, 2018) at the Hartree-Fock (HF) theory level using the 6-31G(d) basis set. Subsequently, we computed the single-point energy calculation using the local MØller-Plesset second-order perturbation (LMP2) method and the correlation-consistent polarized valence cc-pVTZ(-f) basis set. We then computed partial charges computed by fitting the molecular electrostatic potential (ESP) at the atomic centers. This LMP2/cc-pVTZ(-f)//HF/6-31G(d) method is one of the common practices for OPLS-AA parameterization[32]. For the biaryl torsional energetics, we utilized the values for biphenyl published by Jorgensen's group in PPPPP force field[33]. Finally, we slightly adjusted the vDW parameters for C and H using ForceBalance[34] to fit two experimental density data point values for PPPPPP[18].

We carried out all simulations using GROMACS[35] version 2018 with GPU acceleration at constant atmospheric pressure by Parrinello-Rahman barostat and temperature by Nose-Hoover thermostat. We employed periodic boundary conditions with a cut-off of 1.5 nm for evaluating the LJ interactions and a fast smooth particle mesh Ewald method for electrostatic interactions with a cut-off of 1.5 nm. We converted all bonds to constraints with Linear Constraint Solver (LINCS) algorithm. We studied a sample of 1000 molecules contained in a cubic cell under NPT conditions in a series of cooling runs. Starting at 750 K in isotropic phase, we allowed the cell to slowly cool down (in 5 K increments) to 653 K. At each temperature setting, we equilibrated the cell for 10ns and another 10ns for production run.

### Appendix A: Tables of NMR splittings and MD simulation data

Table 1: NMR experimental data and order parameters as a function of temperature. These data include the raw NMR quadrupole splittings ( $\Delta v_Q$ ) for each label position and the bond order

parameters S obtained by taking the ratio of the observed splitting and the principal component of the C-D quadrupole tensor  $Q_p$  (**Figure 4**). We obtain the corrected  $S_{zz}$  points for PPP-d<sub>4</sub>PP from the MD simulated  $\cos^2\theta$  parameter, where  $\theta$  is the bond angle with respect to the director axis. We also include the dipole-dipole (D-D) splittings for the PPP-d<sub>4</sub>PP molecule, and the extracted biaxiality parameter obtained by combining the D-D and C-D coupling data for that molecular segment (the central ring). The biaxiality of the electric field gradient tensor for aromatic C-D deuterons is  $\sim 0.05[14, 15]$ , which we have neglected in this analysis. The error estimated in the stated  $S_{xx}$ - $S_{yy}$  biaxiality by NMR is of order  $\pm 0.05$ . Thus, the (molecular segment) biaxiality parameters measured by NMR for the central ring of the PPP-d<sub>4</sub>PP molecule are not significantly different from zero. Note also that the dipole-dipole couplings reported for PPP-d<sub>4</sub>PP ( $\Delta v_{DD}$ ) and extracted from fits to spectra in Figure 5 are the full width D-D spectral splittings between two D-D dipolar split lines one would observe if there were no quadrupole splitting present, and where the internuclear vector is along  $B_0[36]$ .

We obtain the remaining values given in this table as follows: (1) **5 (expt)** for d-PPPPP-d is simply the  $\Delta v_Q$  value measured for this label position divided by the  $Q_p$  extracted from the SSNMR powder spectrum, which is 256 kHz. (2) Similarly, **5 (expt)** for PPP-d<sub>4</sub>PP is simply the  $\Delta v_Q$  value measured for this label position (negative splitting due to  $\theta > 54.7^{\circ}$ ) divided by the  $Q_p$  extracted from the SSNMR powder spectrum, which is 254.8 kHz. (3)  $S_{zz}$  (corrected) for PPP-d<sub>4</sub>PP is the **5 (expt)** value divided by  $P_2(cos\theta)$  with  $\langle cos^2\theta \rangle = 0.230$  obtained from MD simulations. (4) We extract  $S_{xx}$  for PPP-d<sub>4</sub>PP using  $\Delta v_Q = Q_p[S_{zz}\langle cos^2\theta \rangle + S_{xx}\langle sin^2\theta \rangle]$  where  $Q_p = 254.8$  kHz,  $\langle sin^2\theta \rangle = 0.775$  and  $\langle cos^2\theta \rangle = 0.230$  from MD simulations, and  $S_{zz}$  obtained from the D-D coupling on the central ring divided by the dipolar coupling prefactor 0.402 kHz that incorporates  $\langle \frac{1}{r_{D-D}^3} \rangle = 0.0710$  from MD simulations.

d-PPPP-d

Temp (K)	Reduced T	S (expt)	Δν <sub>Q</sub> (kHz)
664	0.9566	0.6230	159.5
668	0.9624	0.5996	153.5
672	0.9682	0.5742	147
676	0.9739	0.5469	140
680	0.9797	0.5156	132
684	0.9854	0.4785	122.5

694	0.9999	0.0000	0
692	0.9970	0.3438	88
688	0.9912	0.4297	110

### PPP-d<sub>4</sub>PP

Temp (K)	Reduced T	S (expt)	Szz (corrected)	$\Delta v_Q$ (kHz)	$\Delta v_{DD}$ (kHz)	$S_{xx}$	$S_{xx}-S_{yy}$
663	0.9470	-0.0834	0.5383	21.26	0.248	-0.2179	0.1051
669	0.9556	-0.0788	0.5082	20.07	0.236	-0.2071	0.0964
674	0.9627	-0.0748	0.4826	19.06	0.226	-0.1980	0.0888
679	0.9699	-0.0705	0.4550	17.97	0.207	-0.1822	0.0927
684	0.9770	-0.0659	0.4249	16.78	0.198	-0.1736	0.0796
689	0.9841	-0.0603	0.3889	15.36	0.181	-0.1588	0.0732
694	0.9913	-0.0528	0.3406	13.45	0.158	-0.1387	0.0649
696	0.9941	-0.0487	0.3142	12.41	0.148	-0.1296	0.0566
698	0.9970	-0.0434	0.2800	11.06	0	N/A	N/A
699	0.9984	-0.0402	0.2595	10.25	0	N/A	N/A
700	0.9999	-0.0314	0.2026	8.00	0	N/A	N/A

Table 2: MD simulation order parameter and density data as a function of temperature.

These data are the  $P_2$  and  $P_4$  order parameters for the **k** axis (*para* axis of the central ring of PPPPP) from simulations, along with the density. The MD simulated (phase) biaxiality parameters extracted from the C-H bond position in the central ring of PPP-d<sub>4</sub>PP, which involve errors from the limited number of molecules in the simulation box as well as uncertainty in the definition of the nematic director in the simulation, are not significantly different from zero. However, we note that the trends of both NMR-derived and simulated biaxialities are sensible in that they are largest at the bottom of the nematic T range and they decrease with increasing T.

(k axis)						(central ring C-H)	
	Temp (K)	Reduced T	P <sub>2</sub>	$P_4$	Density (kg/m³)	S <sub>xx</sub> -S <sub>yy</sub> (biaxiality)	
	663	0.9512	0.8258	0.5823	954.9		
	664	0.9527	0.6793	0.3401	926.5	0.0312	
	665	0.9541	0.6707	0.3233	924.7	0.0313	
	668	0.9584	0.6568	0.3067	920.3	0.0312	
	670	0.9613	0.6508	0.2994	918.2	0.0324	
	672	0.9641	0.6351	0.2822	914.8	0.0314	
	675	0.9684	0.6178	0.2626	911.3	0.0310	
	676	0.9699	0.6170	0.2623	910.3	0.0316	

MD simulations

MD simulations

680	0.9756	0.5859	0.2311	904.5	0.0311
684	0.9813	0.5670	0.2105	899.2	0.0304
685	0.9828	0.5543	0.2050	898.3	0.0289
688	0.9871	0.5279	0.1803	893.6	0.0294
690	0.9900	0.4889	0.1506	889.4	0.0277
692	0.9928	0.4498	0.1294	885.4	0.0249
695	0.9971	0.3335	0.0730	877.8	0.0165
700	1.0043	0.1985	0.0329	868.0	0.0062
710	1.0187	0.0758	0.0163	855.3	-0.0022
720	1.0330	0.0593	0.0100	843.5	
740	1.0617	0.0161	0.0067	820.9	

## Appendix B: Equations used for extracting bond order parameters from NMR

The following expression describes the quadrupolar splitting associated with the C-D bond of a non-rigid molecule

$$\Delta v_Q = \frac{3}{2} q_{CD} \left[ \langle P_2 (\hat{B} \cdot \hat{e}_{CD}) \rangle + \frac{\eta_{EFG}^{CD}}{3} \langle P_2 (\hat{B} \cdot \hat{e}'_{CD}) - P_2 (\hat{B} \cdot \hat{e}''_{CD}) \rangle \right]$$

where  $\hat{B}$  is the direction of the spectrometer field,  $\eta_{EFG}^{CD}$  is the biaxiality of the electric field gradient tensor and  $\hat{e}_{CD}$ ,  $\hat{e}'_{CD}$ , and  $\hat{e}''_{CD}$  are the directions of the three principal axes of that tensor.

This is the expression we use in this paper, with  $\eta^{C\,D}_{EFG}$  taken as negligible. A similar expression is used for the dipolar couplings:  $D_{ij} = -K_{ij} \, \langle \frac{P_2(\hat{B}\cdot\hat{r}_{ij})}{r_{ij}^3} \rangle$ . Note that the dipolar splitting tabulated above  $\Delta v_{DD}$  is twice the  $D_{ij}$  mentioned here. In this way, the measured spectral quantities  $\Delta v_Q$  and  $D_{ij}$  for specific deuterium labels are related to the local segmental order parameters of the flexible molecule obtained by molecular dynamics simulations.

## Appendix C: Synthesis details of deuterated quinquephenyl mesogens

Two deuterium labelled *p*-quinquephenyl derivatives, *p*-quinquephenyl-*d4* and *p*-quinquephenyl-*d2*, were prepared using deuterated aromatic precursors and the synthetic procedures are summarized in Schemes 1 and 2. Replacing all four protons on the central *p*-quinquephenyl ring could be achieved in one step. Two equivalents 4-biphenylboronic acid were

coupled with 1,4-dibromobenzene-*d4* using Suzuki cross coupling chemistry, as shown in Scheme 1. The target compound, *p*-quinquephenyl-*d4*, was obtained in near quantitative yield.

**Scheme 1.** Synthetic scheme towards *p*-quinquephenyl-*d4*. Perdeuterated 1,4-dibromobenzene is coupled with 2 equivalents of biphenyl boronic acid using Suzuki cross coupling conditions.

Placing deuterium at the *para*-position of the *p*-quinquephenyl terminal phenyl units proved to be more challenging. Our attempt to prepare 4'-*d*-4-biphenylboronic acid failed because the precursor 4'-*d*-4-bromobiphenyl was difficult to isolate in high purity. It appeared much easier to prepare a Grignard reagent of 1,4-dibromobenzene followed by a D<sub>2</sub>O quench as this yields 4-*d*-bromobenzene that could easily be isolated from the reaction mixture (Scheme 2A). This intermediate was converted to 4-*d*-phenylboronic acid and subsequently coupled with 4,4"-dibromo-*p*-terphenyl under Suzuki cross coupling conditions to yield *p*-quinquephenyl-*d*2 (Scheme 2B).

A

Br 
$$\frac{1-1 \text{ eq. Mg/THF}}{2-D_2O}$$
 Br  $\frac{1-1 \text{ eq. Mg/THF}}{2-B_2O}$   $\frac{1-1 \text{ eq. Mg/THF$ 

**Scheme 2.** Synthetic scheme towards *p*-quinquephenyl-*d2*. Deuterium is introduced at the *para*-position of the terminal phenyl units by coupling 2 equivalents of phenyl boronic acid-d with 4,4"-dibromo-*p*-terphenyl using Suzuki cross coupling conditions.

### **Experimental details**

Tetrahydrofuran (THF) and dimethoxyethane (DME) were dried over and distilled from sodium/benzophenone prior to use. All start materials (4-biphenylboronic acid, 1,4-dibromobenzene-*d4*, 1,4-dibromobenzene and 4,4"-dibromo-*p*-terphenyl) and reagents (Mg, D<sub>2</sub>O, trimethylborate, sodium carbonate and Pd(PPh<sub>3</sub>)<sub>4</sub>) were purchased from Sigma-Aldrich and used as received. All soluble intermediates were confirmed using <sup>13</sup>C-NMR spectroscopy. The spectra were collected with a Bruker Avance 300 spectrometer (300 MHz). Mass spectra (MS) were obtained using a Waters Integrity MS system; M<sup>+</sup> representing the molecular ion. Transition temperatures were determined with a Perkin Elmer Pyris differential scanning calorimeter, calibrated with indium (99.99%)(m.p. 156.5 °C, ΔH=28.315 J/g) and tin (99.99%)(m.p. 232.0 °C, ΔH=54.824 J/g). Heating and cooling scans were recorded at 10 °C under a nitrogen atmosphere. All samples were encapsulated in hermetically sealed aluminum sample pans to prevent samples sublimation.

## Synthesis and characterization of *p*-quinquephenyl-*d4*

A 100 mL two-neck round-bottom flask equipped with magnetic stir bar, reflux condenser, and argon gas inlet was charged with 1,4-dibromobenzene-d4 (1.20 g, 5 mmol) and 3 mol% tetrakis(triphenylphosphine)palladium(0) (0.34 g, 0.3 mmol). A volume of 20 mL dimethoxyethane (DME) was added and the bright yellow solution was allowed to stir for 10 min at room temperature. 4-Biphenylboronic acid (2.38 g, 12 mmol) and 20 mL of 2 M Na<sub>2</sub>CO<sub>3</sub> were added and the resulting reaction mixture was refluxed for 24 h. under an argon atmosphere. After cooling the reaction mixture to room temperature, 50 mL water was added and the solids were washed with water (3X), acetone (3X) and dichloromethane (3X) and vacuum dried overnight at 60 °C. The crude product was dissolved in 1,2,4-trichlorobenzene and hot filtered over a short patch of silica gel and celite. Pure p-quinquephenyl-d4, 1.85 g (97%), was obtained as colorless platelets after 3 recrystallizations from hot 1,2,4-trichlorobenzene. Low-resolution MS: 386 (M+), 306, 193, 149, 57. DSC (second heat, peak maxima are reported): K–N (391.0 °C,  $\Delta$ H<sub>f</sub> = 63.44 KJ mol<sup>-1</sup>), N–I (418.4 °C,  $\Delta$ H<sub>f</sub> = 0.94 KJ mol<sup>-1</sup>).

## Synthesis and characterization of *p*-quinquephenyl-*d2*

4-d-Bromobenzene: A flame-dried 300 mL 3-neck round bottom flask equipped with a heavy magnetic stir bar, reflux condenser, and argon gas inlet was charged with 1,4-dibromobenzene (25 g, 0.106 mol) and 100 mL anhydrous THF. Magnesium (powder) (1.22 g, 0.05 mol) was slowly added in order to control the exotherm. After 1h. the reaction mixture was cooled to 0 °C on an ice-bath and 2 mL D<sub>2</sub>O was added dropwise in order to quench the Grignard. After stirring the reaction mixture for another 30 min, THF was removed using a rotary evaporator. Ice water (50 mL) was slowly added to the crude product and the suspension was allowed to stir and warm-up to room temperature over 1h. The water/oil mixture was extracted with diethyl ether (3X) and the organic layer was dried over anhydrous MgSO<sub>4</sub>. Diethyl ether was removed using a rotary evaporator and the resulting oil was dissolved in anhydrous ethanol and the solution was cooled to -10 °C to allow residual 1,4-dibromobenzene and 1,4-benzene-d2 to crystallize. Pure 4-d-bromobenzene, 5.2 g (66%), was obtained as a colorless liquid after a fractional distillation (fraction collected between 155 and 158 °C) of the residue under atmospheric pressure. <sup>13</sup>C NMR (75.48 MHz, DMSO-d<sub>6</sub>) δ 121.7 (C-Br), 126.7, 127.0, 127.3 (C-D), 130.4 (meta to C-Br), 131.2 (ortho to C-Br); Low-resolution MS: 158 (M+), 78, 51.

4-d-Phenylboronic acid: A flame dried 100 mL two-neck round-bottom flask equipped with magnetic stir bar, reflux condenser, and argon gas inlet was charged with 4-d-bromobenzene (4.6 g, 30 mmol) and 40 mL anhydrous THF. Mg (0.71 g, 30 mmol) was slowly added in order to control the exotherm. After all Mg was added, the reaction mixture was refluxed for 4 h. The Grignard solution was cooled to room temperature and added slowly to a cooled (-78 °C) trimethyl borate solution (6.23 g, 60 mmol in 15 mL anhydrous THF) and the resulting reaction mixture was allowed to warm-up to room temperature overnight. The resulting reaction mixture was acidified with 10 mL of a 10% HCl solution and stirred for 1 h. at room temperature. The crude product was extracted into diethyl ether (3 X 50 mL) and washed with a saturated Na<sub>2</sub>CO<sub>3</sub> solution and water. The water was removed using a rotary evaporator and the crude 4-d-phenylboronic acid was recrystallized twice from water/ethanol (95/5) and used immediately for the next step. Yield: 2.1 g (57%).

p-quinquephenyl-d2: A 100 mL two-neck round-bottom flask equipped with magnetic stir bar, reflux condenser, and argon gas inlet was charged with 4,4"-dibromo-p-terphenyl (1.94 g, 5 mmol) and 3 mol% tetrakis(triphenylphosphine)palladium(0) (0.34 g, 0.3 mmol). A volume of 20 mL dimethoxyethane (DME) was added and the yellow solution was allowed to stir for 10 min at room temperature. 4-d-Phenylboronic acid (1.47 g, 12 mmol) and 20 mL of 2 M Na<sub>2</sub>CO<sub>3</sub> were added and the resulting reaction mixture was refluxed for 24 h. under an argon atmosphere. After cooling the reaction mixture to room temperature, 50 mL water was added and the solids were washed with water (3X), acetone (3X) and dichloromethane (3X) and vacuum dried overnight at 60 °C. The crude product was dissolved in 1,2,4-trichlorobenzene and hot filtered over a short patch of silica gel and celite. Pure p-quinquephenyl-d2, 1.81 g (94%), was obtained as colorless platelets after 3 recrystallizations from hot 1,2,4-trichlorobenzene. Low-resolution MS: 384 (M+), 307, 192, 149, 71, 57. DSC (second heat, peak maxima are reported): K–N (391.3 °C,  $\Delta$ H<sub>f</sub> = 67.34 KJ mol<sup>-1</sup>), N–I (420.9 °C,  $\Delta$ H<sub>f</sub> = 1.22 KJ mol<sup>-1</sup>).

## **Appendix D: Diffusion coefficient computations for PPPPP**

In order to assess diffusion lengths and director fluctutations, we have simulated diffusion in PPPPP as a function of T, as shown in **Figure 12**. We used the GROMACS diffusion module to determine mean-square displacement, from which we extract the diffusion coefficient D.

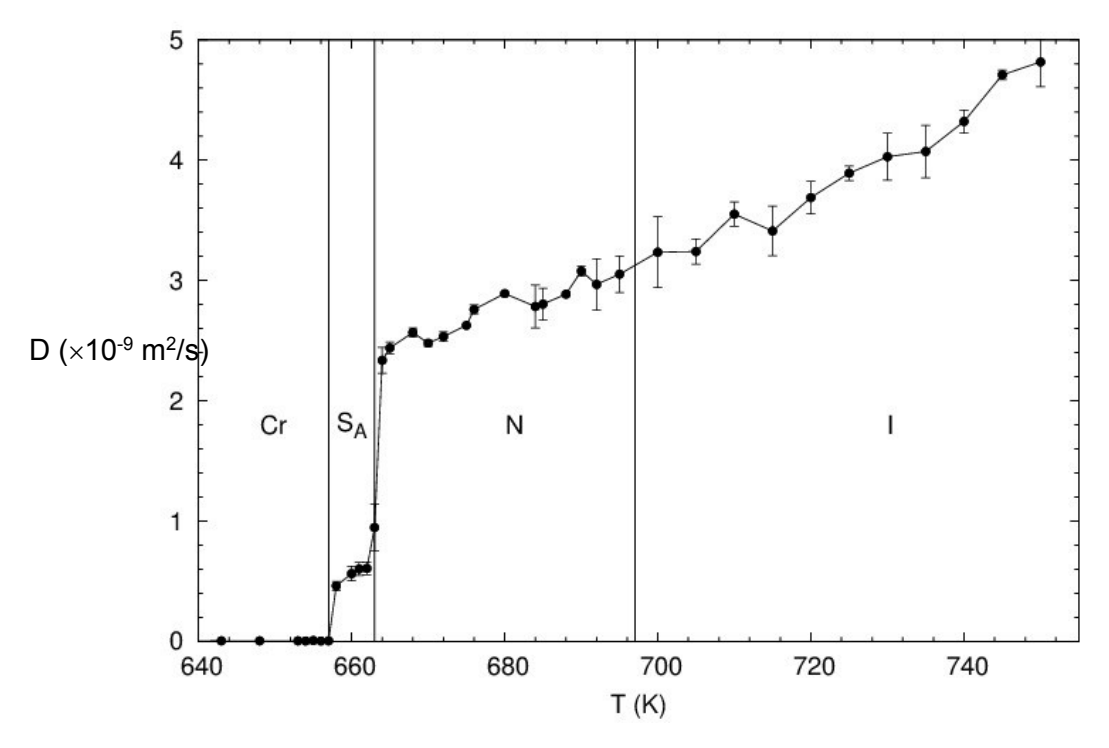


Figure 12: PPPPP diffusion coefficient versus absolute temperature from MD simulations.

## Acknowledgements

The authors wish to thank Professor Zeev Luz and the wonderful community of scientists he supported and spawned, for expanding our scientific horizons and our understanding of dynamics in oriented phases. We are also indebted to Professor Demetri Photinos for clarifying discussions.

### **Funding**

This work was supported in part by the US National Science Foundation (NSF) under Award DMR-1810194.

#### References

## References

- 1. Onsager L. The Effects of Shape on the Interaction of Colloidal Particles. An. N. Y. Acad. Sci. 1949;51:627-59.
- 2. Flory PJ. Phase equilibria in solutions of rod-like particles. Proc. R. Soc. Lond. Ser. A Math. Phys. Sci. 1956;234:73-89.
- 3. Flory PJ, Ronca G. Theory of Systems of Rodlike Particles: I. Athermal systems. Molec. Cryst. Liq. Cryst. 1979;54:289-309.

- 4. Warner M. A New Theory of the Equilibrium Properties of Nematic Liquid Crystals. Molec. Cryst. Liq. Cryst. 1982;80:79-104.
- 5. Maier W, Saupe A. Eine einfache molekular-statistische Theorie der nematischen kristallinflüssigen Phase. Teil II. Zeitschrift für Naturforschung A1960. p. 287.
- 6. Maier W, Saupe A. Eine einfache molekular-statistische Theorie der nematischen kristallinflüssigen Phase. Teil l. Zeitschrift für Naturforschung A1959. p. 882-7.
- 7. Maier W, Saupe A. Eine einfache molekulare Theorie des nematischen kristallinflüssigen Zustandes. Zeitschrift für Naturforschung A1958. p. 564.
- 8. Dingemans TJ, Madsen LA, Zafiropoulos NA, et al. Uniaxial and biaxial nematic liquid crystals. Phil. Trans. R. Soc. A Math. Phys. Eng. Sci. 2006;364:2681-96.
- 9. Kuiper S, Norder B, Jager WF, et al. Elucidation of the Orientational Order and the Phase Diagram of p-Quinquephenyl. J. Phys. Chem. B. 2011;115:1416-21.
- 10. Olivier Y, Muccioli L, Zannoni C. Quinquephenyl: The Simplest Rigid-Rod-Like Nematic Liquid Crystal, or is it? An Atomistic Simulation. ChemPhysChem. 2014;15:1345-55.
- 11. Emsley JW. Measurement of Orientational Ordering by NMR. In: Emsley JW, editor. Nuclear Magnetic Resonance of Liquid Crystals. NATO ASI Series. Dordrecht, Holland: D. Reidel; 1985. p. 379-412.
- 12. Spiess HW, Schmidt-Rohr KS. Multidimensional Solid-State NMR and Polymers London: Academic Press; 1994.
- 13. Poupko R, Vold RL, Vold RR. Density matrix calculations of the relaxation of two deuterons in an ordered medium. J. Magn. Reson. (1969). 1979;34:67-81.
- 14. Heist LM, Poon CD, Samulski ET, et al. Benzene at 1GHz. Magnetic field-induced fine structure. J. Magn. Reson. 2015;258:17-24.
- 15. Pyykkö P, Elmi F. Deuteron quadrupole coupling in benzene: librational corrections using a temperature-dependent Einstein model, and summary. The symmetries of electric field gradients and conditions for  $\eta = 1$ . Phys. Chem. Chem. Phys. 2008;10:3867-71.
- 16. Eppenga R, Frenkel D. Monte Carlo study of the isotropic and nematic phases of infinitely thin hard platelets. Molec. Phys. 1984;52:1303-34.
- 17. Komolkin AV, Laaksonen A, Maliniak A. Molecular dynamics simulation of a nematic liquid crystal. J. Chem. Phys. 1994;101:4103-16.
- 18. Irvine PA, Wu DC, Flory PJ. Liquid-crystalline transitions in homologous p-phenylenes and their mixtures. Part 1.—Experimental results. J. Chem. Soc., Faraday Trans. 1: Phys. Chem. in Condens. Ph. 1984;80:1795-806.
- 19. Wang Y, Gao J, Dingemans TJ, et al. Molecular Alignment and Ion Transport in Rigid Rod Polyelectrolyte Solutions. Macromol. 2014;47:2984-92.
- 20. Chowdhury S, Madsen LA, Frazier CE. Probing Alignment and Phase Behavior in Intact Wood Cell Walls Using H-2 NMR Spectroscopy. Biomacromol. 2012;13:1043-50.
- 21. Li J, Park JK, Moore RB, et al. Linear coupling of alignment with transport in a polymer electrolyte membrane. Nat. Mater. 2011;10:507-11.
- 22. Deloche B, Samulski ET. Short-Range Nematic-Like Orientational Order in Strained Elastomers A Deuterium Magnetic-Resonance Study. Macromol. 1981;14:575-9.
- 23. Callaghan PT. Translational dynamics and magnetic resonance: Principles of pulsed gradient spin echo NMR. Oxford; New York: Oxford University Press; 2011.
- 24. Luckhurst GR, Fukuda A, Dunmur D. Physical properties of liquid crystals : nematics. 2001.

- 25. Peroukidis SD, Vanakaras AG, Photinos DJ. Molecular simulation study of polar order in orthogonal bent-core smectic liquid crystals. Phys. Rev. E. 2015;91:062501.
- 26. Vanakaras AG, Photinos DJ. Thermotropic biaxial nematic liquid crystals: Spontaneous or field stabilized? J. Chem. Phys. 2008;128:154512.
- 27. Gelbart WM. Molecular theory of nematic liquid crystals. J. Phys. Chem. 1982;86:4298-307.
- 28. McColl JR, Shih CS. Temperature Dependence of Orientational Order in a Nematic Liquid Crystal at Constant Molar Volume. Phys. Rev. Lett. 1972;29:85-7.
- 29. deGennes PG, Prost J. The Physics of Liquid Crystals. 2nd ed. New York: Oxford University Press; 1993.
- 30. Slichter CP. Principles of Magnetic Resonance. 3rd ed. New York: Springer-Verlag; 1990.
- 31. Dodda LS, Cabeza de Vaca I, Tirado-Rives J, et al. LigParGen web server: an automatic OPLS-AA parameter generator for organic ligands. Nucleic Acids Res. 2017;45:W331-W6.
- 32. Kaminski GA, Friesner RA, Tirado-Rives J, et al. Evaluation and Reparametrization of the OPLS-AA Force Field for Proteins via Comparison with Accurate Quantum Chemical Calculations on Peptides. J. Phys. Chem. B. 2001;105:6474-87.
- 33. Dahlgren MK, Schyman P, Tirado-Rives J, et al. Characterization of Biaryl Torsional Energetics and its Treatment in OPLS All-Atom Force Fields. J. Chem. Inf. Model. 2013;53:1191-9.
- 34. Wang L-P, Martinez TJ, Pande VS. Building Force Fields: An Automatic, Systematic, and Reproducible Approach. J. Phys. Chem. Lett. 2014;5:1885-91.
- 35. Van Der Spoel D, Lindahl E, Hess B, et al. GROMACS: Fast, flexible, and free. J. Comput. Chem. 2005;26:1701-18.
- 36. Dong RY. Nuclear magnetic resonance of liquid crystals. 2nd ed. New York: Springer; 1997.